Short Communication

Accelerated Durability Testing and Partition Analysis of Gas Diffusion Layer for Proton Exchange Membrane Fuel Cell

Zhen Li[1], Shang Li[1,2,], Kuangwei Cheng[1], Wei Yan[1], Zhen Zhu[1], Mu Pan[1,2]*

[1] State Key Laboratory of Advanced Technology for Materials Synthesis Processing, Wuhan University of Technology, Wuhan 430070, People's Republic of China
[2] Foshan Xianhu Laboratory of the Advanced Energy Science and Technology Guangdong Laboratory, Xianhu Hydrogen Valley, Foshan 528200, People's Republic of China
*E-mail: lishang@whut.edu.cn

In this paper, the durability of a gas diffusion layer was investigated using potentiostatic methods. The gas diffusion layer was successfully isolated after durability testing, and its degradation at different locations was characterized by the limiting-current method, scanning electron microscopy, and contact angle measurement. The results demonstrate that the most substantial degradation of the gas diffusion layer occurs at the air inlet as evidenced by the reduction in water discharge ability, a large increase in oxygen transmission resistance, a decrease in hydrophobicity, and a reduction in gas diffusion layer thickness.

1. INTRODUCTION

The advantages of proton exchange membrane fuel cells (PEMFCs) include their light weight, high energy conversion efficiency, and environmental friendliness, but their durability is still an important factor limiting the large-scale application of PEMFCs [1,2]. A full understanding of the degradation mechanism of each PEMFC component is particularly important. A PEMFC is composed of four main components: a bipolar plate, a gas diffusion layer (GDL), a catalyst layer, and a membrane [3]. The GDL is usually composed of substrate and a microporous layer (MPL). The connection between the bipolar plate and the catalytic layer has to ensure that the reaction gas can smoothly reach the catalytic layer from the flow channel of the bipolar plate and that the water generated in the catalytic layer can be discharged at a certain speed. Therefore, the GDL is a key structure to ensure gas distribution and water

management in fuel cells [4]. However, the degradation of the GDL severely restricts the improvement of fuel cell life [5-8].

During the operation of the fuel cell, the GDL is exposed to generated water and humidified water and is easily flooded. Fuel cells are in a complex chemical environment, and a large amount of water will dissolve carbon materials and generate hydroxides, oxides, and other materials [9,10]. Latorrata [11] soaked a GDL in a 20% sulfuric acid solution for 1000 hours. After the experiment, the static contact angle decreased from $158 \pm 2°$ to $147 \pm 5°$, the total weight decreased by about 3%, and surface cracks in the MPL became wider. George [12-15] designed a series of experiments. A GDL was immersed in 35%wt diluted aqueous hydroperoxide (H_2O_2) at 90 °C to accelerate aging. According to the experimental results, the hydrophobicity of the GDL and the mass transmission resistance were significantly reduced. X-ray diffraction analysis and other visualization methods indicated that the liquid water content in the cell increased by 44% under the same current density (2.5 A/cm^2) [12]. Athanasaki [16] used two methods for accelerated testing by immersing a GDL in H_2O_2 (30%wt) at 90 °C for 24 hours or in deionized water at 80 °C for 1000 hours. Both acceleration methods resulted in the generation of cracks on the surface of the MPL, greatly reducing the static contact angle and its porosity; however, the H_2O_2 method caused greater damage to the GDL. High-speed reaction gas flows in the flow channel will result in GDL corrosion. For this reason, Chun [17] designed a 25-cm^2 virtual fuel cell and studied GDL degradation by passing a high-speed flow (10 L/min) of either dry or 100%-humidified air into the fuel cell for 14 days. The comparison revealed that the surface damage of the MPL is mainly caused by water in the humidified air. The high flow rate of dry air did not cause serious damage to the GDL. Furthermore, a reduction in surface cracks can improve its durability. Under the conditions of start/stop, shutdown, or partial hydrogen deficiency during fuel cell operation, a local hydrogen-void interface will be generated, and the local voltage can be higher than 1.5 V [18], causing corrosion of the carbon on the cathode electrode, which can be accelerated by the catalyst of the cathode. Yu [19] used an ex-situ method to study the electrochemical durability of a GDL. Employing a three-electrode system with the GDL as the working electrode, graphite plate and saturated calomel electrode as the counter electrode and reference electrode, respectively, the as-prepared electrode was placed into a 0.5-M sulfuric acid solution, and a constant potential of 1.25 V was applied. The results demonstrated that the carbon material in the GDL was oxidized, the hydrophobicity was lost, and the mass loss of carbon material far exceeded that of polytetrafluoroethylene (PTFE). The above studies on the durability of the fuel cell GDL mostly investigated the degradation behavior of the entire GDL under a single condition. However, due to the complex and non-uniform environment inside the fuel cell, the degradation of various regions may be different.

In this paper, a two-electrode system is established using a fuel cell test platform to perform an accelerated GDL durability test and conduct a spatial study of GDL. Scanning electron microscopy, contact angle measurement, and mercury porosimetry were employed to investigate the degradation and failure mechanism of the GDL cathode inlet, middle, and outlet part. The limiting-current method was used to study the change in oxygen transport resistance in each region of the GDL.

2. EXPERIMENTAL AND THEORY

2.1 Materials and instruments

Commercial catalyst-coated membrane (CCM) was sandwiched between two commercial GDLs to form a membrane electrode assembly (MEA), and the total Pt loading was 0.5 mg/cm^2. The I-V curves were recorded on the MEA with a surface area of 25 cm^2, which was installed in a single cell fixture with a single serpentine flow field. The single cell test was conducted on an HTS-125 fuel cell test station.

The durability test was performed on a Reference 3000 electrochemical workstation (Gamry Instruments, USA). Scanning electron microscopy (SEM) was conducted on an S-4800 instrument (Hitachi, Japan) and a JSM-7500F instrument (JEOL, Japan) to characterize the surface and cross-sectional morphologies of GDLs. The hydrophobicity of GDLs was determined by an XG-CAMD3 automatic contact angle measurement instrument (Shanghai Xuanyichuangxi Industrial Equipment Co., Ltd., China).

2.2 Single cell test and accelerated test

Commercial GDL and CCM assembled into the MEA were named Fresh-0. After the activation test was performed at 0.5 V for 2 hours, the polarization curve was recorded. The cathode GDL of Fresh-0 was removed and assembled with fresh anode GDL and CCM, named Fresh-1. The polarization curve test was performed under the same conditions as used for Fresh-0. The test conditions were as follows: fuel cell temperature of 75 ℃, 100% relative humidity for both cathode and anode, a stoichiometric hydrogen/air ratio of 2.0/2.0, and a backpressure of 150 kPa. Data points are recorded every two minutes.

The accelerated test (AST) was performed on the Fresh-1 MEA by applying a constant potential of 1.6 V on the cathode for 36 hours. During the AST, the cathode of the battery was fed with a nitrogen flow of 1000 sccm, while a hydrogen flow of 800 sccm was used for the anode. The relative backpressure of the cathode and anode was 150 kPa, and cathode and anode gas was 50%-humidified.

After AST, the cathode GDL was removed from Fresh-1, and GDLs of a size of 2 cm × 1 cm were cut off from the inlet, middle, and outlet points. Those aged GDLs and a fresh cathode GDL were assembled into MEAs with the same area of fresh CCMs and anode GDLs, named Inlet, Mid, Outlet, and Fresh, respectively. The performance test and oxygen transport resistance test were conducted on those MEAs. The conditions for the two tests are listed in Table 1 and Table 2, respectively.

The limiting-current measurements of these MEAs were performed with hydrogen flowing into the anode and nitrogen-diluted oxygen gas flowing into the cathode of the HTS-125 fuel cell test station, as described by Wan [20]. The cell voltage ranged from 0.7 to 0.05 V, and the current at 0.05 V was selected as the limiting current density (I_{lim}).

Table 1. Performance test conditions of the 2-cm^2 single cell

Test Conditions	HEPHAS (HTS-125)
Cell temperature/°C	75
Relative backpressure/kPa	150
Relative Humidity RH/%	100
Anode flow/(mL/min)	500
Cathode flow/(mL/min)	1000

Table 2. Oxygen transport resistance test condition

Test Conditions	HEPHAS (HTS-125)
Cell temperature/°C	75
Gas relative pressure/kPa	150
Relative Humidity RH/%	70
Oxygen mole fraction/%	0.5, 1.0, 1.5, 2.0, 4.0, 8.0, 12.0, 16.0, 21.0
Anode flow/(mL/min)	1600
Cathode flow/(mL/min)	4600

According to references [17,21,22], the total oxygen transfer resistance, R_{total}, can be calculated from the limiting current density by the following equation:

$$R_{total} = \frac{4FX_{O_2}^{dry,in}}{I_{lim}} \frac{P-P^w}{RT} \tag{1}$$

Here, F is the Faraday constant, $X_{O_2}^{dry,in}$ is the oxygen mole fraction, T is the cell thermodynamic temperature, P is the total gas pressure, P^w is the partial pressure of water vapor, and R is the ideal gas constant, I_{lim} is the current density corresponding to the cell at 0.05 V.

3. RESULTS AND DISCUSSION

3.1 Polarization curve

To study the effect of separation and reassembly on fuel cell performance, the polarization curves of Fresh-0 and Fresh-1 were recorded. The curves in Fig. 1 demonstrate that the separation and reassembly process did not affect the performance of the fuel cell. This separation method can be used to analyze GDL degradation.
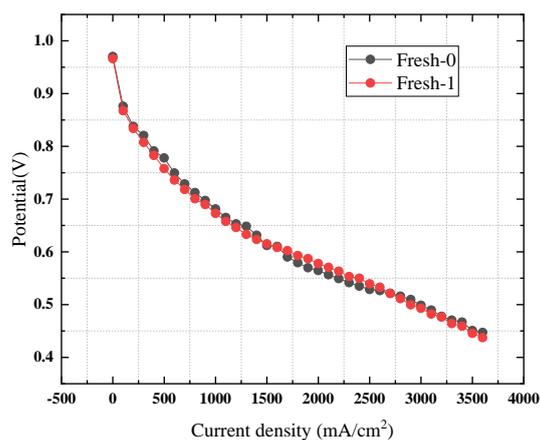
Figure 1. Polarization curves of MEAs before and after reassembly (cell temperature: 75 °C; relative humidity at cathode and anode: 100%; hydrogen/air stoichiometric ratio: 2.0/2.0; backpressure: 150 kPa).
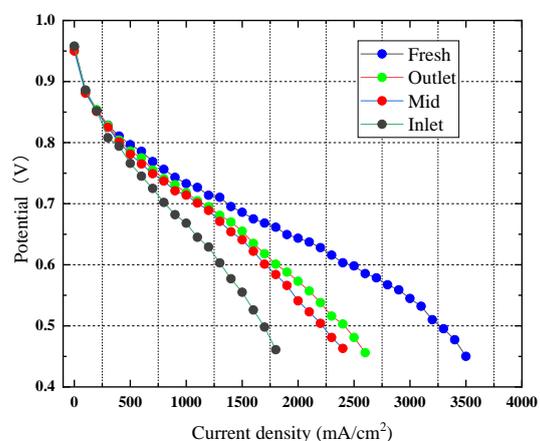

Figure 2. Polarization curve of single cells (cell temperature: 75 °C; relative humidity at cathode and anode: 100%; hydrogen flow: 500 sccm; air flow: 100 sccm; backpressure: 150 kPa).

Fig. 2 shows the polarization curves of Fresh, Outlet, Mid, and Inlet cells. There is no obvious difference among the four curves in the open-circuit voltage and electrochemical polarization region (potential > 0.85 V). The voltage in these regions was determined by the CCM and was not influenced by the GDL. However, when the voltage was lower than 0.85 V, the performances of the MEAs with GDLs after AST significantly decreased, especially under high current densities. This deterioration was caused by an increase in the concentration polarization and a severe decrease in the water management capability of GDLs after the durability test. At high current densities, the fuel cell produced a lot of water and flooded, which eventually caused the observed performance degradation. A number of researchers have observed a decline in the water management capacity of aged GDLs [17,19-21]. However, This

paper observes the degree of GDL degradation was not the same in the different GDL areas and was most serious at the air inlet position and weaker at the middle and outlet positions.

2.2 Oxygen transfer resistance

     A decrease in the water management capability of the GDL will lead to an increase in oxygen transfer resistance. Fig. 3 displays the limiting current densities under different oxygen concentrations. At low oxygen concentrations (dry oxygen mole fraction < 2%), the cell was relatively dry, oxygen diffusion was only affected by the pore structure, and the limiting current density linearly increased with the increase in oxygen concentration. However, when the oxygen concentration was high, the water generated in the MEA could not be effectively discharged, and the limiting current density approached a plateau. Reaching this plateau at higher oxygen concentrations indicates better water management capability of the GDL. Wang [23] defined the R_{total} constant region as the dry region, the R_{total} growth region as the wet region and defined the current density value corresponding to the R_{total} growth exceeding 5% as the dry-wet boundary. In this paper, the dry region of the three aged GDLs became smaller, and the air inlet position was the smallest. At an oxygen concentration of 21%, the limiting current densities of the MEAs composed of GDLs after AST were significantly reduced. Compared to the fresh GDL, the limiting current densities of the inlet, outlet, and middle positions dropped by 2000, 800, and 1100 mA/cm^2, respectively. Fig. 4 shows the total oxygen transfer resistance R_{total} as a function of limiting current density. Similar to its highest decrease in limiting current density performance, the GDL at the inlet also exhibited the highest R_{total}, which increased by 92.28 s/m compared to the Fresh sample.
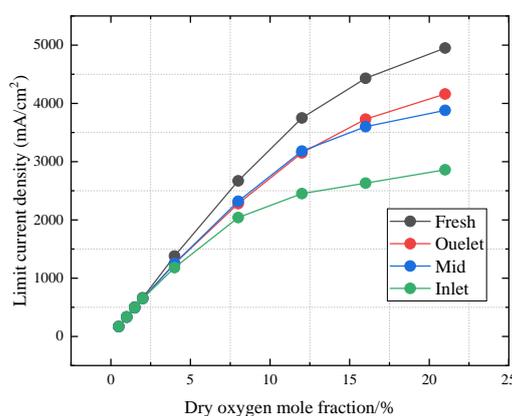

Figure 3. Limiting current density curves (cell temperature: 75 °C; cathode gas flow: 1600 sccm; anode gas flow: 4600sccm; relative humidity at cathode and anode: 70%; relative gas pressure: 150 kPa).
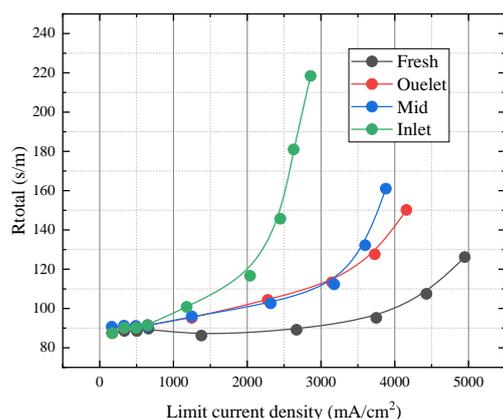
Figure 4. Oxygen transport resistance curves (cell temperature: 75 °C; cathode gas flow: 1600 sccm; anode gas flow: 4600sccm; relative humidity at cathode and anode: 70%; relative gas pressure: 150 kPa).

2.3 Scanning electron microscopy

The GDL degradation is typically caused by considerable damage to its surface and internal structure. As shown in Fig. 5, the GDL surface of the Fresh-MPL (a) has small cracks of 5-10 μm in width, the Outlet-MPL (b) has a surface structure similar to the Mid-MPL (c) with a crack width of 10-30 μm, and the corrosion of Inlet-MPL (d) is the most severe with a crack width of more than 50 μm. The wide cracks indicate that carbon in MPL was corroded at high potential. The air with high flow rates at the inlet repeatedly scoured the cracks and widened them. Cross-sectional micrographs of substrate layers are shown in Fig. 6(a-d). After AST, the layer was thinned at different points, particularly at the air inlet position, where the thickness was reduced by 35.5%. The great reduction in the width of the substrate layer will lead to its poor mechanical properties and weakened supporting capacity. In his research on the resistance of GDL to airflow erosion [17], Chun observed many holes in the GDL after airflow erosion. However, in this experiment, erosion was manifested as the expansion of cracks, which probably were mainly the result of electrochemical corrosion and water dissolution.
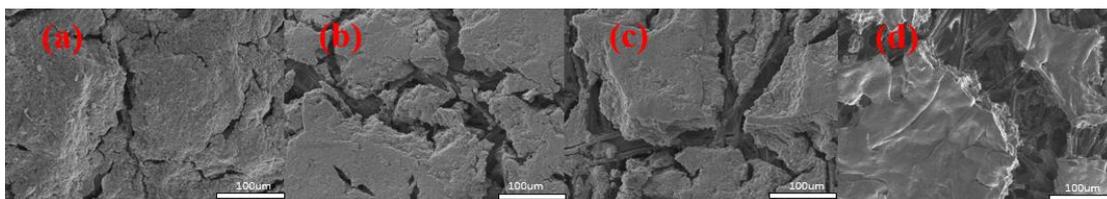

Figure 5. SEM surface micrographs of gas diffusion layers: surface of (a) Fresh-MPL; (b) Outlet-MPL; (c) Mid-MPL; (d) Inlet-MPL (accelerating voltage: 5 kV; magnification factor: 300).
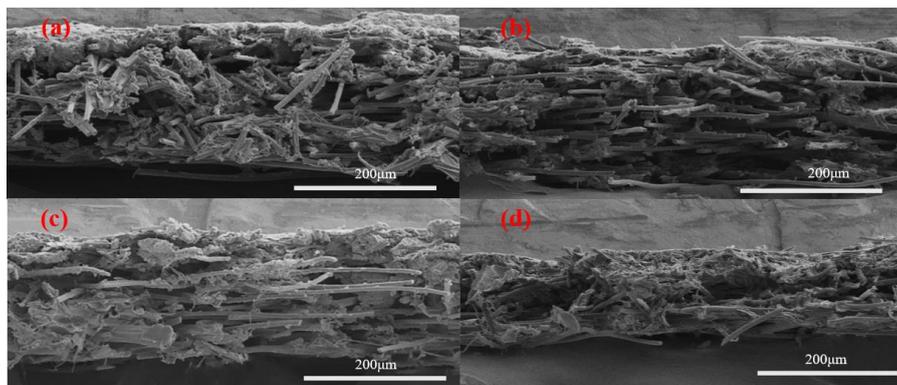
Figure 6. Cross-sectional SEM micrographs of (a) Fresh; (b) Outlet; (c) Mid; (d) Inlet samples (liquid nitrogen brittle fracture; accelerating voltage: 5 kV; magnification factor: 200).

During the early stages of AST, water electrolysis is the dominant process in the MEA. However, the conservation of electric charge cannot be sustained when the water content in the MEA declines over time, and then carbon oxidation reaction occurs. Notably, the carbon corrosion potential is much lower than the water electrolysis potential, which means that carbon corrosion preferentially occurs thermodynamically; however, since the water electrolysis reaction is kinetically much faster, this reaction is predominantly observed [24,25]. Aslam [6] found that the water content in the air outlet of the MEA is much higher than that in the air inlet. Therefore, the carbon corrosion at the outlet is more severe.

2.4 Hydrophobicity of MPL

The hydrophobicity of MPL surfaces is an important indicator for evaluating GDLs. Chen [26] confirmed that in the same type of GDL, the hydrophobicity of the GDL increases with increasing PTFE content. Yu [19] found that the loss of carbon materials in the GDL after electrochemical corrosion is much greater than the loss of PTFE, and the hydrophobicity of the GDL surface is reduced. Therefore, the reduced hydrophobicity of the GDL may be caused by the change in the material structure. There are two main hydrophobicity models on rough surfaces: Wenzel state and Cassie state. As shown in Fig. 8(a), Wenzel introduced the roughness factor (*r*) into Young's equation and established the Wenzel equation (Eq. (2)) to describe the behavior of a material surface when it was completely wetted:

$$cos\emptyset_w = rcos\emptyset_0 \tag{2}$$

In Eq. (2), $\emptyset_0$ is the apparent contact angle, namely Young's contact angle, *r* (*r* > 1) is the roughness factor, and $\emptyset_w$ is the Wenzel contact angle. The roughness factor *r* can be regarded as an amplification factor. The contact angle increases with increasing surface roughness of the hydrophobic material. In the Wenzel state, the liquid and the solid are completely wetted. A binding force is generated at the interface, which prevents the droplet from rolling freely. Cassie improved the Wenzel model, as shown in Fig. 8(b), by considering the contributions of both gas phase and solid phase components, which resulted in the Cassie equation (Eq. (3)).

$$cos\emptyset_c = f_{aL}cos\emptyset_{aL} + f_{vL}cos\emptyset_{vL} \tag{3}$$

In Eq. (3), $\emptyset_c$ is the Cassie contact angle; f_{aL} and f_{vL} are the ratios of the solid-liquid and gas-liquid contact areas to the total wetting area, respectively; $\emptyset_{aL}$ is the apparent contact angle of the solid-liquid interface; $\emptyset_{vL}$ is the gas-liquid apparent contact angle of the gas-liquid interface. When the wetted state is in the Cassie state, the presence of the gas-liquid interface can result in apparent contact angles larger than 150°. Since the solid is not fully wetted in this state, the liquid can roll when tilted at a small angle.
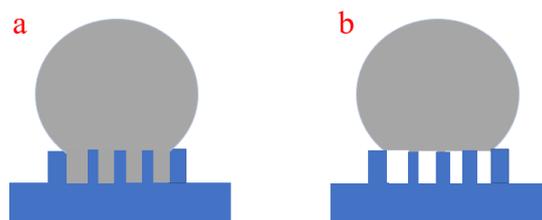

Figure 7. Schematic diagram of the solid surface wetting states: (a) Wenzel state; (b) Cassie state.

Fig. 8 shows the static contact angles of new MPL and post-AST MPL at different positions. Since the surface contact angle of MPL is much higher than that of pure PTFE (about 110°), its hydrophobicity is the result of the combined effect of the material hydrophobicity of PTFE and the structural hydrophobicity of MPL. Its wetting behavior can be explained by these two models. The surface of Fresh-MPL (Fig. 8a) exhibited the largest static contact angle and the strongest droplet-rolling ability, which conforms to the Cassie model. In the MPL after AST, the contact angle was smaller, the surface droplet-rolling ability was weak, and the wetting behavior changed to the Wenzel state. Combined with the SEM results, Outlet-MPL was smoother in non-crack regions than Fresh-MPL, and the roughness factor *r* decreased, which resulted in a decrease in the static contact angle (Fig. 8b). However, in the intermediate position (Fig. 8c) and the inlet position (Fig. 8d), the increase in the number and widths of cracks caused a decrease in the hydrophobic surface and, consequently, in the contact angle.
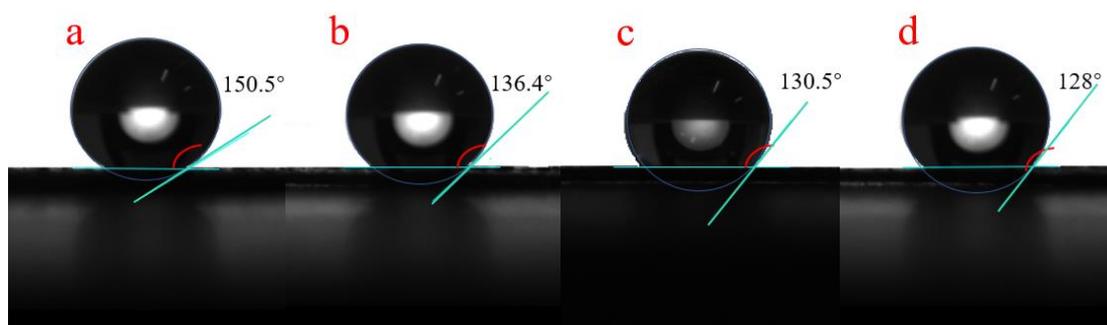

Figure 8. Contact angles of the fresh and aged MPLs: (a) Fresh-MPL; (b) Outlet-MPL; (c) Mid-MPL; (d) Inlet-MPL (ambient temperature: 25 °C; water volume: 5 μL).

4. CONCLUSION

In this work, the durability of a GDL was investigated in a PEMFC using potentiostatic methods. The GDL was successfully isolated after durability testing, and the degradation of GDL at different locations was characterized. The decline in the water management ability of the GDL after durability testing mainly originated from the decrease in the hydrophobicity of the microporous layer and the weakening of the supporting ability of the base layer. The degradation degree of GDL was the largest at the air inlet followed by the middle position, and the degradation degree at the air outlet was the smallest. The destruction of the MPL surface and structure was an important factor for the decrease in its hydrophobicity. After durability testing, the wetting behavior on the MPL surface changed from Cassie state to Wenzel state, and the contact angle decreased.

References

1. H. Wang, A. Gaillard and D. Hissel, *Int. J. Hydrogen Energy*, 44(2) (2019) 1110-1121.
2. A. Kongkanand and M.F. Mathias, *J. Phys. Chem. Lett.*, 7(7) (2016) 1127-1137.
3. F. Mojica, Md. A. Rahman, J. M. Mora, J. D. Ocon and P.Y.A. Chuang, *Feul Cells*, 20(5) (2020) 547-557.
4. J.F. Wu, J.J. Martin, F.P. Orfino, H. Wang, C. Legzdins, X.Z. Yuan and C. Suna, *J. Power Sources*, 195(7) (2010) 1888-1894.
5. H. Zhang, L. Xiao, P.Y.A. Chuang, N. Djilali and P.C. Chieh, *Appl. Energy*, 251 (2019) 113316.
6. C. Cai, Y. Rao, Y. Zhang, F. Wu, S. Li and M. Pan, *Int. J. Hydrogen Energy*, 44(26) (2019) 13786-13793.
7. M. Bosomoiu, G. Tsotridis and T. Bednarek, *J. Power Sources*, 285 (2015) 568-579.
8. J. Cho, T. Ha, J. Park, H.S. Kim, K. Min, E. Lee and J.Y. Jyoung, *Int. J. Hydrogen Energy*, 36(10) (2011) 6090-6098.
9. J. Chlistunoff, J.R. Davey, K.C. Rau, R. Mukundan and R.L. Borup, *ECS Trans.*, 50(2) (2013) 521.
10. Y. Hiramitsu, H. Sato, K. Kobayashi and M. Hori, *J. Power Sources*, 196(13) (2011) 5453-5469.
11. S. Latorrata, P.G. Stampino, C. Cristiani and G. Dotelli, *Chemical Engineering Transactions*, 41 (2014) 241-246.
12. H. Liu, M.G. George, N. Ge, D. Muirhead, P. Shrestha, J. Lee, R. Banerjee, R. Zeis, M. Messerschmidt, J. Scholta, P. Krolla and A. Bazylak, *J. Electrochem. Soc.*, 165(6) (2018) F3271.
13. H. Liu, M.G. George, N. Ge, R. Banerjee, S. Chevalier, J. Lee, P. Shrestha, D. Muirhead, J. Hinebaugh, R. Zeis, M. Messerschmidt, J. Scholta and A. Bazylak, *ECS Trans.*, 75(14) (2016) 289.
14. H. Liu, M.G. George, R. Banerjee, N. Ge, J. Lee, D. Muirhead, P. Shrestha, S. Chevalier, J. Hinebaugh, R. Zeis, M. Messerschmidt, J. Scholta and A. Bazylak, *J. Electrochem. Soc.*, 164(7) (2017) F704.
15. M.G. George, H. Liu, D. Muirhead, R. Banerjee, N. Ge, P. Shrestha, J. Lee, S. Chevalier, J. Hinebaugh and M. Messerschmidt, *J. Electrochem. Soc.*, 164(7) (2017) F714.
16. G. Athanasaki, N. Chauhan, R. Ahmad and A.M. Kannan, *Int. J. Hydrogen Energy*, 46(62) (2021) 31754-31763.

17. J.H. Chun, D.H. Jo, S.G. Kim, S.H. Park, C.H. Lee and S.H. Kim, *Renewable Energy*, 48 (2012) 35-41.
18. D.R. Baker, C. Wieser, K.C. Neyerlin and M.W. Murphy, *Ecs Trans.*, 3(1) (2006) 989.
19. S. Yu, X. Li, S. Liu, J. Hao, Z. Shao and B. Yi, *RSC Adv.*, 4(8) (2014) 3852-3856.
20. Z. Wan, Q. Zhong, S.F. Liu, A.P. Jin, Y.N. Chen, J. Tan and M. Pan, *Int. J. Hydrogen Energy*, 42(6) (2018) 2225-2233.
21. J.P. Owejan, T.A. Trabold and M.M. Mench, *Int. J. Heat Mass Transfer*, 71 (2014) 585-592.
22. H. Oh, Y.il. Lee, G. Lee, K. Min and S.Y. Jung, *J. Power Sources*, 345 (2017) 67-77.
23. S. Wang, X. Li, Z. Wan, Y. Chen, J. Tan and M. Pan, *J. Power Sources*, 379 (2018) 338-343.
24. T.W. Patterson and R.M. Darling, *Electrochem. Solid-State Lett.*, 9(4) (2006) A183.
25. S.D. Knights, K.M. Colbow, J. St-Pierre and D.P. Wilkinson, *J. Power Sources*, 127(1-2) (2004) 127-134.
26. T. Chen, S. Liu, J. Zhang and M. Tang, *Int. J. Heat Mass Transfer*, 128 (2019) 1168-1174.